INTERNATIONAL JOURNAL FOR NUMERICAL METHODS IN FLUIDS
Int. J. Numer. Meth. Fluids 2006; **52**:801–821
Published online 15 March 2006 in Wiley InterScience (www.interscience.wiley.com). DOI: 10.1002/fld.1210

Numerical simulation of unconfined flow past a triangular cylinder

Arnab Kumar De*,† and Amaresh Dalal‡

Department of Mechanical Engineering, Indian Institute of Technology Kanpur, Kanpur, India

SUMMARY

Numerical simulations of two-dimensional laminar flow past a triangular cylinder placed in free-stream at low Reynolds number ($10 \leqslant Re \leqslant 250$) are performed. A finite volume method, second-order accurate in space and time, employing non-staggered arrangement of the variables with momentum interpolation for the pressure–velocity coupling is developed. Global mode analysis predicts $Re_{cr} = 39.9$ which confirms the results of earlier studies. Vortex shedding phenomena is found to be similar to the square cylinder with no second bifurcation in the range of Re studied. A discussion on the time-averaged drag coefficient, rms of lift coefficient and Strouhal number is presented. Particle tracking and the instantaneous streaklines provide an excellent means of visualizing the von Kármán vortex street. Copyright © 2006 John Wiley & Sons, Ltd.

KEY WORDS: triangular cylinder; onset of vortex shedding; pathlines; streaklines; laminar vortex shedding

1. INTRODUCTION

Flow around bluff bodies has been a topic of intense research for the last 100 years owing to its applications with engineering significance. Electronic cooling, heat exchanger systems, structural design, acoustic emission are a few to name. It also embodies a great deal of academic interest due to a range of fluid mechanical issues it presents. In recent years, it has received attention in terms of both numerical and experimental studies as a result of ever increasing computational power and advent of new experimental techniques.

It is understood that above a critical Reynolds number, flow around slender cylindrical bodies in general exhibits the well-known time periodic vortex shedding as a result of the

*Correspondence to: Arnab Kumar De, Department of Mechanical Engineering, Indian Institute of Technology Kanpur, Kanpur 208 016, India.
†E-mail: arkde@iitk.ac.in
‡E-mail: amaresh@iitk.ac.in

Received 10 August 2005
Revised 25 January 2006
Accepted 26 January 2006

Bénard–von Kármán instability leading to alternate vortical structures known as the von Kármán vortex street. This phenomena is responsible for fluctuating forces on the body that may cause structural vibrations, acoustic noise emissions and some times resonance triggering the failure of structures. Thus, it is important from engineering point of view to investigate flow around slender bodies with different shapes.

Large number of investigations on flow past circular cylinder have been accomplished in the past by many researchers [1–4]. A thorough review on this topic can be found in References [5, 6]. These works shed light on the behaviour of flow in different regime of Reynolds number, fluctuating forces the body is subject to, flow transition and the modes responsible for it. At the critical *Re*, the twin vortices that form owing to separation become unstable and vortices are shed. The point of separation for circular cylinder moves downstream along the surface as *Re* increases while it is the rear end vertices which remain to be the location of flow separation for square cylinder in the *Re* range close to the critical value. Although, at higher *Re* the separation points move along the horizontal edges. Davis and Moore [7] carried out two-dimensional numerical simulation of flow past a rectangular cylinder for $100 \leqslant Re \leqslant 2800$. One of their findings was Strong dependence of the drag, lift coefficients and Strouhal number on *Re*. Two- and three-dimensional flow past a square cylinder for varying aspect ratios was computed by Tamura and Kuwahara [8]. Okajima [9], through his numerical simulations, showed that there exists a critical range of *Re* in which Strouhal number changes are accompanied by a drastic change in the flow patterns. Linear stability analysis of Kelkar and Patankar [10] gave the critical Reynolds number which marks the onset of vortex shedding to be 53. Sohankar *et al.* [11] provided the force coefficients and Strouhal number for flow past a square cylinder for $45 \leqslant Re \leqslant 250$. Saha *et al.* [12] found the 2D–3D transition to occur at a Reynolds number between 150 and 175. Recently, Sharma and Eswaran [13] reported the study of free-stream flow and heat transfer over a square cylinder with two different thermal extremities.

Jackson [14] examined the onset of periodic behaviour in two-dimensional laminar flow past bodies of various shapes in free stream. He reported the critical Reynolds number as 34.318 and corresponding Strouhal number as 0.13554 for isosceles triangle with base 1 and height 0.8. Zielinska and Wesfreid [15] numerically investigated the wake flow behind an equilateral triangular obstacle with a blockage ratio of 1/15. They found a critical Reynolds number of 38.3 which was further confirmed by the experiments of Wesfreid *et al.* [16]. Abbassi *et al.* [17] studied the structure of laminar flow and heat transfer from a built-in triangular prism placed in a differentially heated channel. The transition from symmetric to periodic flow was observed at $Re = 45$ with a blockage ratio of 1/4. Recently, Johansson *et al.* [18] computed turbulent flow past triangular-shaped flameholders using k–ε model. To the best of our knowledge, laminar flow around triangular cylinder has not been investigated extensively which has mainly motivated the present work.

The organization of the paper is as follows. After a brief statement of the problem, governing equations along with boundary conditions are compiled. In Section 3, a brief discussion on the numerical method is presented which is followed by validation and grid refinement test results. In Section 4, results and discussions, effect of domain size, onset of vortex shedding, steady and periodic flow description, integral force coefficients and wake visualization are dealt separately. The paper ends with the conclusions that summarize the findings.

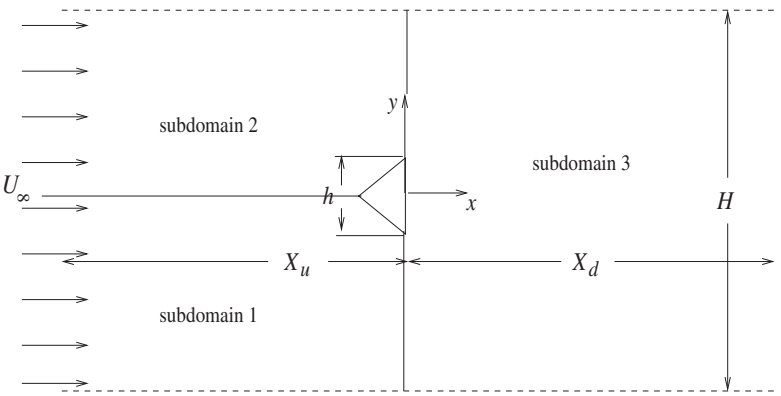

Figure 1. Schematic of the computational geometry.

1.1. Statement of the problem

The present paper focuses on the steady and unsteady flow past an equilateral triangular cylinder of side h placed in uniform stream. Figure 1 shows the geometry in detail. The baseline case involves an upstream length $X_u = 9h$, downstream length $X_d = 20h$ and the free stream situated at a distance of $H = 20h$. These lengths have been varied to see their effects on the quality of solution. Discussions on this issue will be taken up in Section 4.1.

2. GOVERNING EQUATIONS AND BOUNDARY CONDITIONS

The flow is assumed to be two-dimensional, laminar and incompressible with constant fluid properties. The set of governing equations contain two momentum equations and the mass conservation law written in normalized form

$$\frac{\partial u_j}{\partial t} + \frac{\partial (u_j u_k)}{\partial x_k} = -\frac{\partial p}{\partial x_j} + \frac{1}{Re}\frac{\partial^2 u_j}{\partial x_k \partial x_k} \tag{1}$$

$$\frac{\partial u_j}{\partial x_j} = 0 \tag{2}$$

where Reynolds number, $Re = U_\infty h/v$ is defined based on side of the cylinder and free stream velocity. Thus, length and velocity scales used for normalization are h and U_∞, respectively.

Various boundary conditions used in the present simulation are briefly mentioned here.

Inflow plane: Free stream condition for velocity and Neumann boundary condition for pressure is used at the inflow plane

$$u = U_\infty, \quad v = 0 \quad \text{and} \quad \frac{\partial p}{\partial x} = 0$$

Solid boundaries: No-slip condition for velocity and normal gradient condition for pressure is used on the cylinder

$$u = v = 0 \quad \text{and} \quad \nabla p \cdot \hat{n} = 0 \text{ where } \hat{n} \text{ is the normal unit vector}$$

Far field: As the present study focuses on the unconfined flow past a triangular cylinder, a slip free boundary is taken at a distance of $H = 10h$ where Neumann pressure boundary condition is applied

$$\frac{\partial \phi}{\partial y} = 0, \quad \phi = u, v \quad \text{and} \quad \frac{\partial p}{\partial y} = 0$$

Exit boundary: This boundary poses the biggest difficulty in computational modelling of a range of fluid flow problems. Especially flows with unsteady wake or convecting vortices, prescription of this boundary condition is of paramount importance since it not only changes the flow pattern but also affects convergence. Two kinds of boundary conditions at this plane are found to be most applicable. The first one is prescribing the derivative of all the dependent variables to zero. This is known as Neumann boundary condition (NBC)

$$\frac{\partial \phi}{\partial x} = 0, \quad \phi = u, v$$

On the other hand, convective boundary condition (CBC) given by

$$\frac{\partial \phi}{\partial t} + U_c \frac{\partial \phi}{\partial x} = 0, \quad \phi = u, v$$

is found to work quite favourably in terms of passage of vortical structure in undistorted form and smooth convergence. The velocity U_c can be taken as the free stream velocity or an averaged one at the exit, of which the second approach has been adopted in the present calculations. Pressure boundary condition is of Dirichlet type at this plane, $p = 0$.

3. NUMERICAL DETAILS

A finite volume method with non-staggered arrangement of the variables has been developed to solve the set of momentum equations and continuity equation. The computational domain has been divided into three subdomains, as shown in Figure 1, which facilitates the use of structured grids. Pressure velocity coupling is enforced through momentum interpolation. Implicit Crank–Nicolson scheme has been used for the time integration. Convective terms are discretized by a QUICK scheme applied to non-uniform grids while the diffusive terms are discretized by the second-order central difference scheme.

Momentum and continuity equations take the following form when integrated over a finite volume:

$$\frac{u_{iP}^{n+1} - u_{iP}^{n}}{\Delta t} + \frac{1}{2}\left(\sum_f F_f^{n+1} u_{if}^{n+1} + \sum_f F_f^{n} u_{if}^{n}\right) = -\sum_f p_f^{n+1} S_{fi} + \frac{1}{2\,Re}\left(\sum_f F_{dfi}^{n+1} + \sum_f F_{dfi}^{n}\right) \quad (3)$$

$$\sum_f F_f^{n+1} = 0 \quad (4)$$

where P and f denotes the cell centre and the cell faces, respectively. Here indices $i = 1, 2$ correspond to streamwise(x) and cross-stream(y) directions, respectively. In the first step,

a provisional velocity field is computed excluding the pressure in the above equation with mass fluxes taken as the latest available one

$$\frac{u^*_{iP} - u^n_{iP}}{\Delta t} + \frac{1}{2}\left(\sum_f F^{n+1,l}_f u^*_{if} + \sum_f F^n_f u^n_{if}\right) = \frac{1}{2\,Re}\left(\sum_f F^*_{dfi} + \sum_f F^n_{dfi}\right) \tag{5}$$

The face velocities are then calculated by adding a pressure gradient term with the linearly interpolated face values from the provisional velocities

$$u_f = Ł(u^*_P, u^*_{nb}) - \frac{\Delta t}{\rho}(\nabla p)_f \tag{6}$$

where Ł denotes linear interpolation. Thus the mass flux is

$$F_f = F^*_f - \Delta t(\nabla p)_f . \mathbf{S}_f \tag{7}$$

When sum of mass flux calculated from Equation (7) over all the faces of a finite volume is set to zero (Equation (4)) the following equation for the pressure is obtained:

$$\sum_f F^{n+1,l+1}_f = \sum_f F^*_f - \Delta t \sum_f (\nabla p)_f . \mathbf{S}_f = 0 \implies \sum_f (\nabla p) . \mathbf{S}_f = \frac{1}{\Delta t}\sum_f F^*_f \tag{8}$$

Equation (8) is the counterpart of the Poisson equation for pressure correction in SIMPLE-like algorithms. The converged pressure of Equation (8) is used for new estimate of mass flux in Equation (7). Here l denotes the flux loop counter which is iterated until flux converges. The converged mass flux along with the pressure that estimates it correspond to the perfectly divergence free velocity field. These quantities are then used to solve Equation (3) for the velocities u^{n+1} and v^{n+1}. The sequential steps that constitute the solution method is written below

1. Initialize the variables and start with mass flux, $F^{n+1,l}_f = F^n_f$.
2. Solve Equation (5) for u^* and v^*.
3. Compute F^*_f required for the pressure equation.
4. Solve the pressure equation, Equation (8).
5. Estimate new mass flux from Equation (7) and set $l = l + 1$.
6. Repeat steps 2–5 till convergence of the fluxes, $|F^{n+1,l+1}_f - F^{n+1,l}_f| < \varepsilon$.
7. Solve Equation (3) for u^{n+1} and v^{n+1} using converged fluxes and pressure.
8. Set $n = n + 1$ and repeat all the steps 2–7 for the next time step.

All system of simultaneous linear equations arising from Equations (3), (5) and (8) are solved by the SOR technique. The convergence is assessed after each iteration and solution residual (in the root mean square sense) is brought below 10^{-5} for Equations (5) and (8) while 10^{-6} for the flux convergence. In all the calculations reported in the present paper time-dependent solution has been obtained by marching in time with $\Delta t = 0.01$.

Structured grid has been generated in the three subdomains separately using the stretching transformation proposed by Roberts [19] which refines the grid in the vicinity of the solid walls. A typical grid showing the full view as well as a close view is shown in Figure 2.

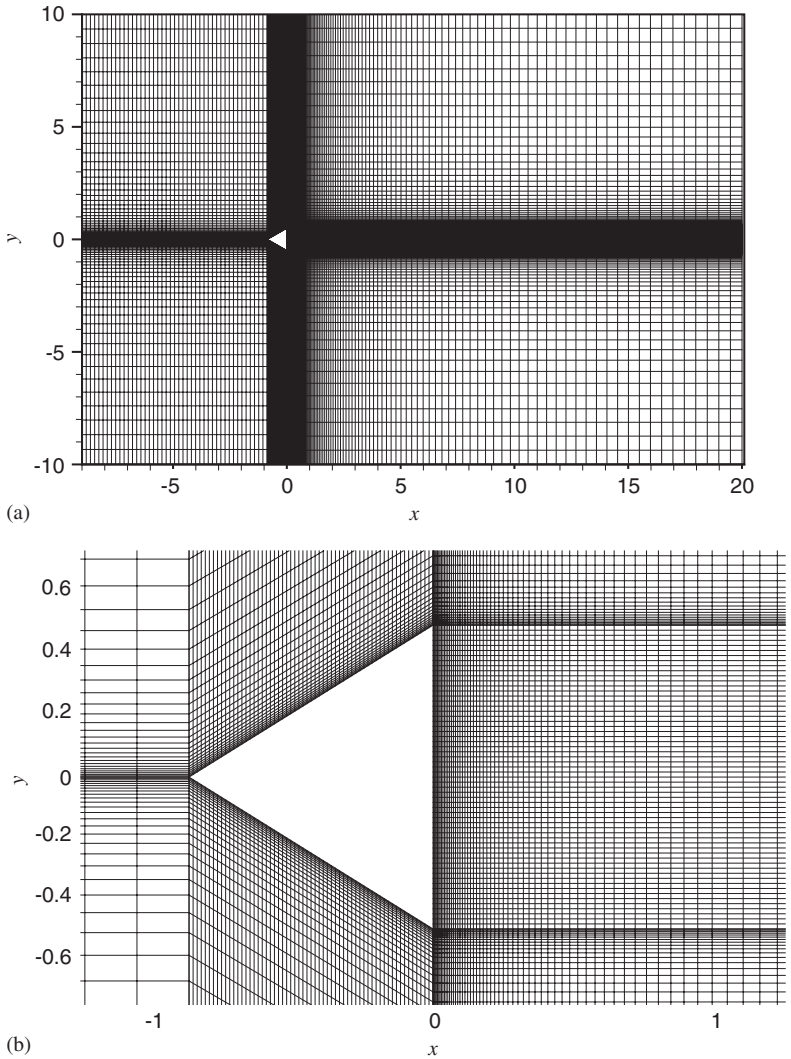

Figure 2. A typical grid (230×160) used in the calculation: (a) full view; and (b) zoomed view.

3.1. Computer code validation

Results obtained with the computer code developed in the present study has been compared with published literatures [11, 13, 20–22] for unconfined flow past square cylinder in the range $10 \leqslant Re \leqslant 200$. While Figure 3(a) shows the comparison for the force coefficients C_D, $C_{L\text{rms}}$, Figure 3(b) shows the comparison for the Strouhal number. It is clear that the present results compare well with the published literatures, especially the rms of the lift coefficient which can be attributed as the most stringent parameter for comparison.

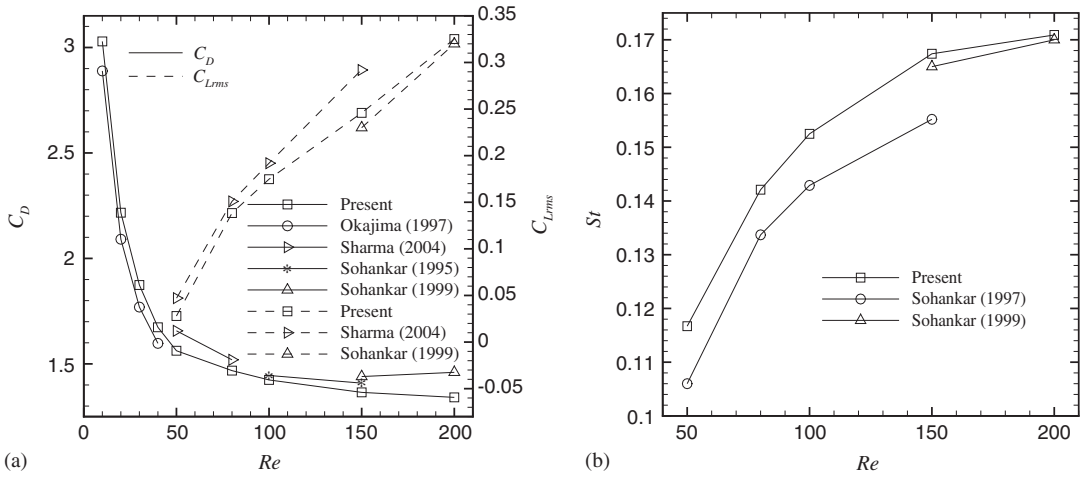

Figure 3. Comparison with published results for square cylinder: (a) C_D and C_{Lrms}; and (b) St.

Table I. Results for grid refinement test with $Re = 100$, $X_u = 9$, $X_d = 20$.

Grid size	C_D	C_{D_p}	$C_{L_{\mathrm{rms}}}$	St
180×120	1.7773	1.3177	0.2963	0.1988
230×160	1.7607 (0.93)	1.3034 (1.09)	0.2968 (0.17)	0.1966 (1.10)
280×200	1.7549 (0.33)	1.2986 (0.37)	0.2974 (0.20)	0.1962 (0.20)

3.2. *Effect of grid refinement*

A grid refinement study has been carried out on three progressively refined grids, namely 180×120, 230×160 and 280×200 where number of grid nodes distributed over a side of the cylinder are 50, 60 and 70, respectively. During the refinement, the smallest and the largest cell size is maintained approximately at $\delta = 0.004$ and $\Delta = 0.5$, respectively. The results are summarized in Table I with percentage change in the parameters written inside the bracket. The variation in C_D, C_{Dp} and St is around 1% when we moved from the coarsest grid level to the intermediate one. But when the grid was further refined, the variation reduced and became close to 0.3%. However, variation in $C_{L\mathrm{rms}}$ remained small during refinement. This has led us to use 230×160 grids for all subsequent calculations.

4. RESULTS AND DISCUSSION

4.1. *Effect of domain size*

In problems with unsteady wake and convecting vortices, length of the downstream section from the bluff body plays a significant role in both quality of the results and the convergence properties. Due to the presence of convecting vortices, too small length of the downstream section can distort the large scale structures. However, as found by Sohankar *et al.* [23], with domain height $H = 20h$, presence of far field boundary hardly influences the flow near

Table II. Results for domain dependence test with $Re = 100$.

Domain length	C_D	C_{D_p}	$C_{L_{\text{rms}}}$	St
$X_u = 6,\ X_d = 15$	1.8168	1.3490	0.3161	0.2021
$X_u = 9,\ X_d = 20$	1.7607 (3.08)	1.3034 (3.38)	0.2968 (6.11)	0.1966 (2.72)
$X_u = 12,\ X_d = 25$	1.7414 (1.10)	1.2879 (1.89)	0.2916 (1.75)	0.1986 (1.02)

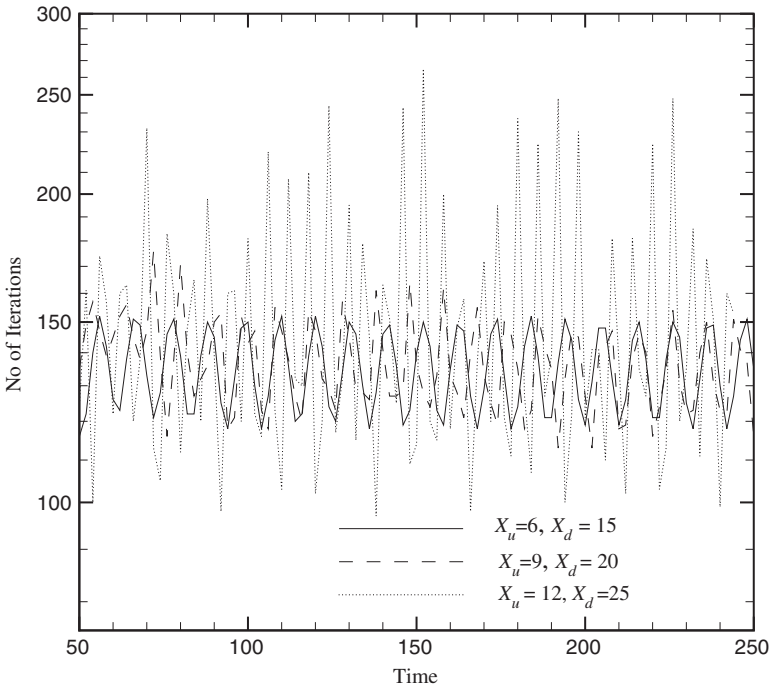

Figure 4. Pressure iterations for cases with different domain size.

the cylinder leading us to use $H = 20h$ in the present study. As reported by a number of research groups [23–27], convective boundary condition (CBC) is less restrictive as compared to the Neumann boundary condition (NBC). It facilitates a smooth passage of the vortices that are shed from the bluff body. In the present study, we have limited ourselves to the use of CBC. Results, summarized in Table II, have been obtained for different upstream and downstream lengths with CBC as the exit boundary condition. In all the calculations the smallest ($\delta = 0.004$) and the largest cell size ($\Delta = 0.5$) have been approximately retained. This has led to use of finer mesh for the case with larger upstream and downstream lengths. The combination $X_u = 6h,\ X_d = 15h$ has been proved to be too restrictive as increasing the sizes leads to considerable changes in the integral parameters as can be seen in Table II. However, increasing the domain size to $X_u = 12h,\ X_d = 25h$ leads to a marginal change (below 2%) in force parameters and St as shown in the table. Figure 4 shows the number of pressure iterations in each time step during the time integration of the momentum equations. With the increase in the domain size, the overall mesh size increases number of iterations required in

each time increment also increases. Thus, effect of total mesh size overrides the advantages obtainable with larger domain size with CBC condition.

4.2. *Onset of vortex shedding*

In wake flows the frequency of oscillations remains the same for a considerable region downstream of the bluff body emphasizing the global nature of the flow dynamics. The experimental studies of Goujon-Durand *et al.* [28] showed that the amplitude of the oscillations has a well defined maximum and its value and position of occurrence depends on *Re* while Dušek *et al.* [29] stressed the importance of the higher nonlinear harmonics in the dynamics of the flow. In the present study, the threshold for vortex shedding has been evaluated using the global modes of u and v velocities on $y = 0$. The procedure used is as follows. We have chosen 30 so-called history points on $y = 0$ at which both u and v velocity signal has been recorded. Figure 5(a) shows the peak to peak amplitude for u and v velocities at the history

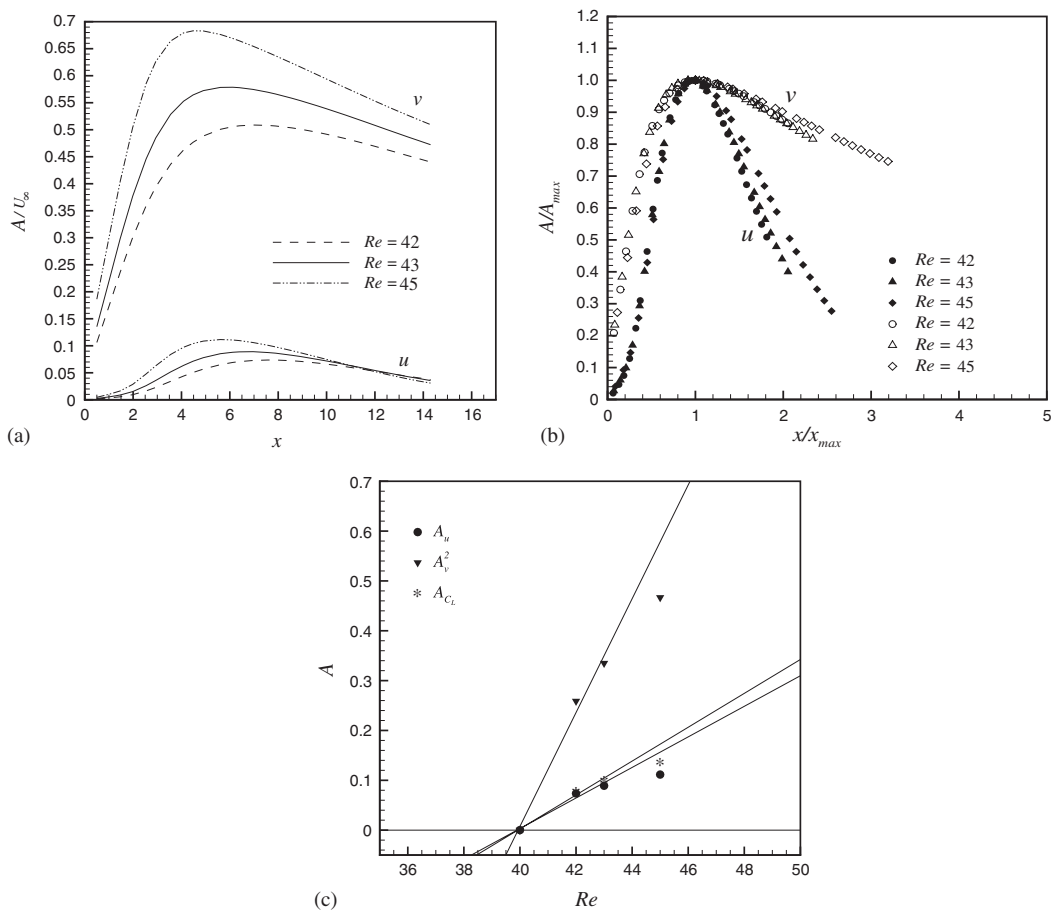

Figure 5. (a) Amplitude of oscillations for u and v velocities on $y = 0$; (b) renormalized global modes; and (c) $A_{\max}$ for u and C_L, $A^2_{\max}$ for v as a function of *Re*.

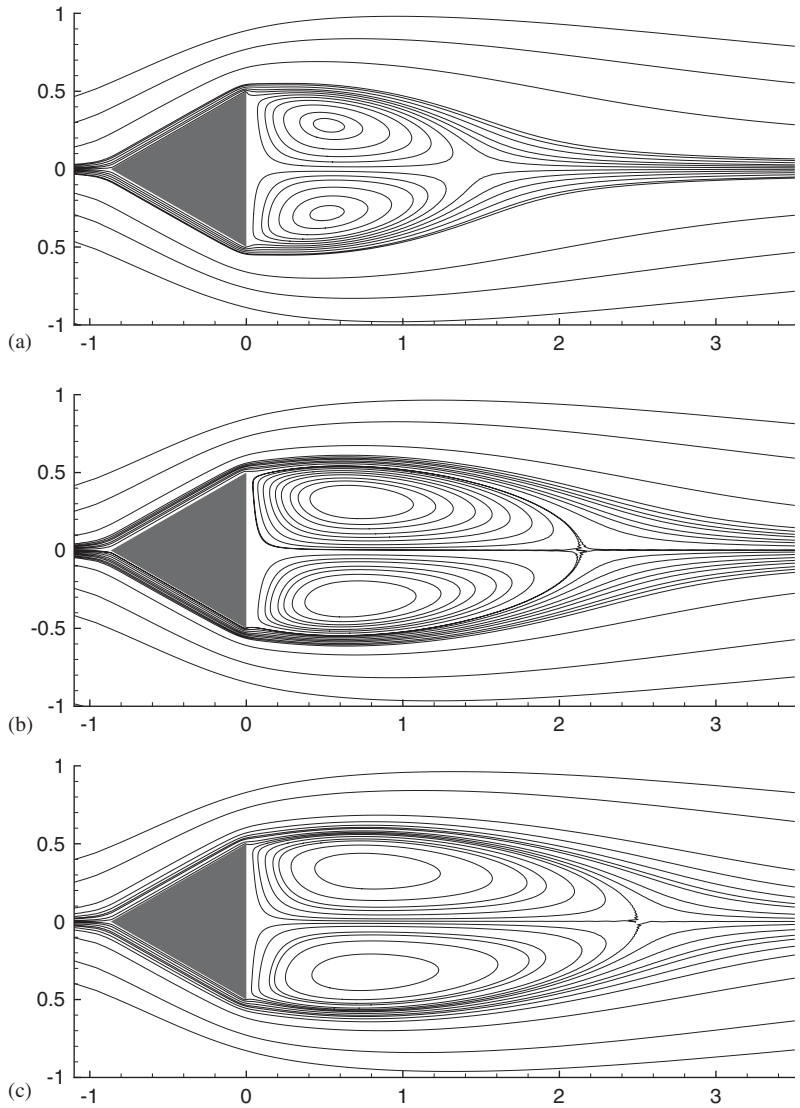

Figure 6. Steady state streamlines: (a) $Re = 20$; (b) $Re = 30$; and (c) $Re = 35$.

points at three different Re close to Re_{cr}. Amplitude of oscillations for both u and v velocities, in all cases, increases in the downstream direction and after reaching a maximum value decreases. The value of the maximum amplitude and its position is different for u and v velocities and depends on Re. Following Goujon-Durand *et al.* [28], amplitude and its position has been renormalized by A_{max} and x_{max}, respectively. It has been found that the normalized curves for different Re collapse to a universal form (see Figure 5(b)). This shows the global nature of the wake whose properties are largely independent of the shape of the bluff body and downstream velocity distribution. The functional relationship between the maximum

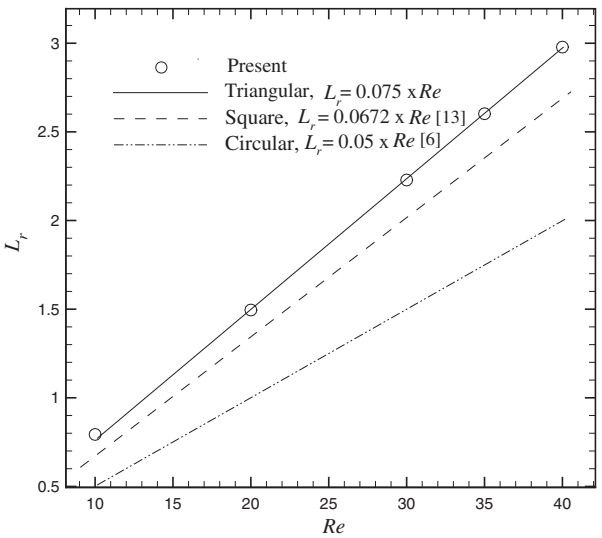

Figure 7. L_r–Re relationship for different bluff configurations.

amplitude and Reynolds number has been used to extract the critical behaviour. Following Dušek *et al.* [29], A_{max} for u and A^2_{max} for v has been used to predict the critical Reynolds number. A linear fit, as shown in Figure 5(c), gives $Re_{cr} = 39.9$ which is obtained by extrapolating the value of $A_{max}(A^2_{max})$ to zero. The peak to peak amplitude of lift coefficient at the saturation state has also been plotted against Re which predicts the same Re_{cr} as can be seen from Figure 5(c). The predicted value of Re_{cr} is higher than $Re_{cr} = 35$ obtained by Jackson [14] who used a blockage ratio of 1/15. Zielinska and Wesfreid [15] found the value of Re_{cr} to be 38.3 while it was 39.6 in the numerical and theoretical study of Dušek *et al.* [29]. The difference between these values can be attributed to the use of different grid, blockage ratio and the effect of sharp edges of the cylinder.

4.3. Steady and unsteady periodic flow

Figure 6 shows the streamline plots in the vicinity of the cylinder at $Re = 20$, 30 and 35. At this subcritical range two steady symmetrical vortices form behind the cylinder whose size increases with increase in Re. Recirculation length (L_r), defined by the reattachment of the fluid layer separated from the two rear-end vertices of the cylinder, has been obtained by monitoring the streamwise velocity along the line of symmetry. The extent of recirculation region spreads with increase in Reynolds number as can be seen from the figure. A linear L_r–Re relationship has been obtained by least square fit, shown below with other bluff configurations

$$\frac{L_r}{h} = 0.05 \times Re \quad \text{for } 4.4 \leqslant Re \leqslant 40, \text{ circular cylinder [6]}$$

$$\frac{L_r}{h} = 0.0672 \times Re \quad \text{for } 5 \leqslant Re \leqslant 40, \text{ square cylinder [13]}$$

$$\frac{L_r}{h} = 0.075 \times Re \quad \text{for } 10 \leqslant Re \leqslant 40, \text{ triangular cylinder, Present}$$

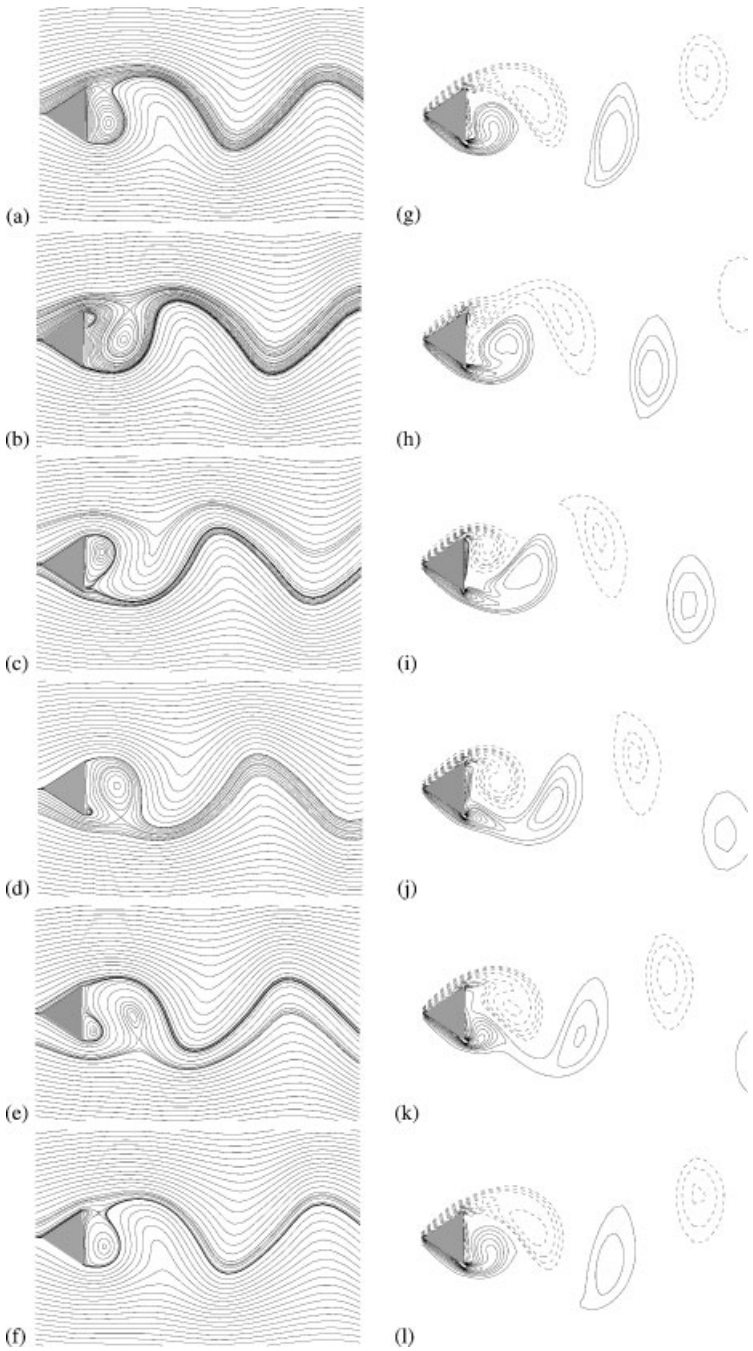

Figure 8. Equispaced ($\theta/6$) snapshots within a shedding cycle, $Re = 100$.

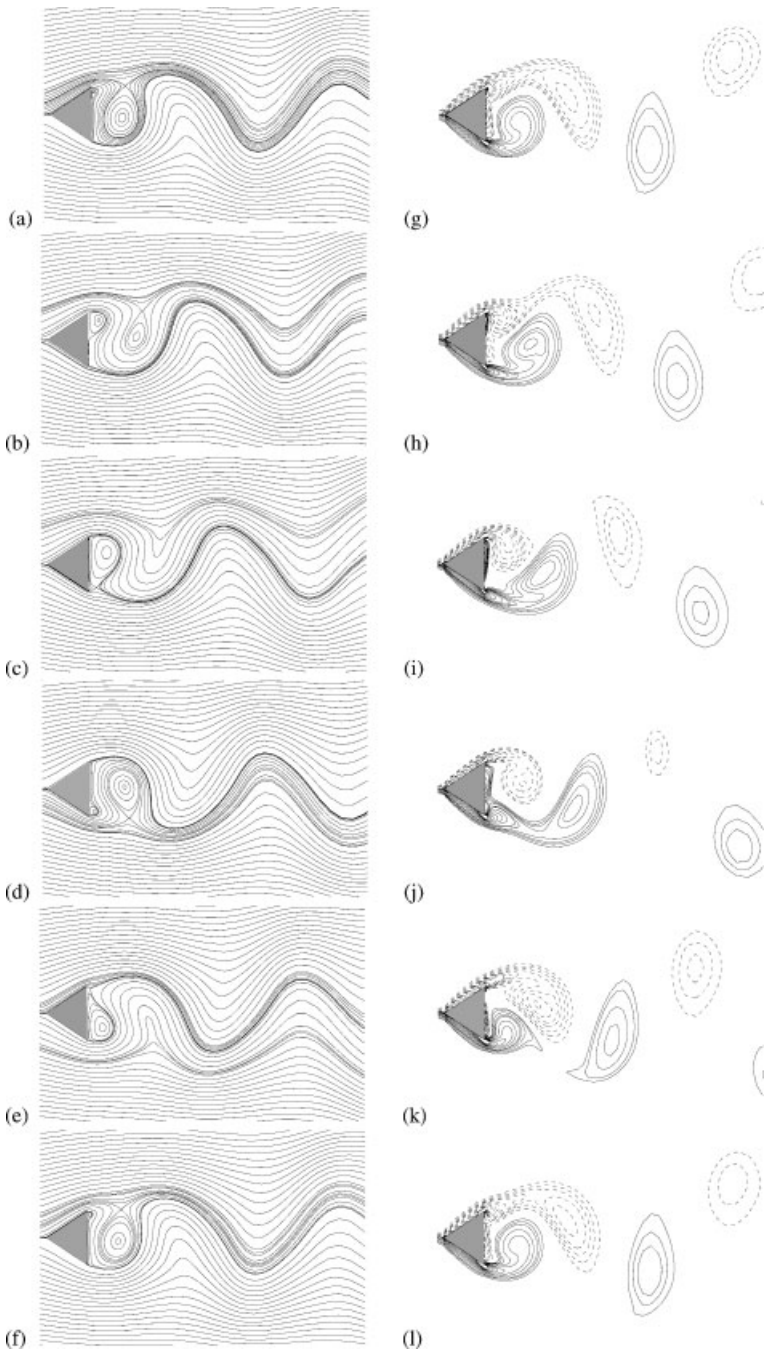

Figure 9. Equispaced ($\theta/6$) snapshots within a shedding cycle, $Re = 150$.

It is clear from Figure 7 that the recirculation length for triangular cylinder is considerably larger than that of circular cylinder but only marginally higher than that of square cylinder.

The flow becomes unsteady and periodic around $Re = Re_{cr}$. In this study, the supercritical range simulated is $50 \leqslant Re \leqslant 250$. Laminar vortex shedding is described here with the help of instantaneous streamlines and vorticity contours corresponding to six equispaced instants within a shedding cycle. Two vortices form at the rear-end vertices of the cylinder and are shed alternately in the wake, as can be seen in Figure 8. Two types of inviscid critical points, namely 'centre' and 'saddle' can be seen from the figure. A critical point, following Perry *et al.* [30] and Eaton [31], is a location where slope of streamline becomes indefinite with the point of zero velocity is referred to as the 'centre' while the point where two stream lines intersect is referred to as the 'saddle'. In the present study, at $Re = 100$, the saddle and centre of a shed vortex disappear before a new vortex is shed. This observation is consistent with Eaton [31] but contrary to Perry *et al.* [30] where coexisting centres and saddles were found. This shows the similarity in vortex shedding mechanism for circular, square and triangular cylinder, at least in the lower range of supercritical region of *Re*. Instantaneous vorticity contours, shown in Figure 8 further reveals the alternate formation and shedding of vortices from the rear-end vertices of the cylinder. Due to its streamlined shape, separation in a triangular cylinder always occurs at the rear-end vertices leading to two separated shear layers from the two vertices that are stretch, bend and finally disconnect into the wake. The neck between the tip and the main body of a growing vortex stretches and bend leading to separation from the main body. The positive and negative vorticity, corresponding to counter-clockwise and clockwise motion, shown by solid and dashed lines, respectively, alternatively engulf the rear end of the cylinder. These layers exhibit a flapping motion while the shear layers moves into the wake only to be convected downstream in the form of vortical structure which scales with the side of the cylinder. These vortices remain in the same half about the centreline from where they are shed. Same mechanism and features of vortex shedding has been found for $Re = 150$ and 200, shown in Figures 9 and 10, respectively. The results at $Re = 250$, shown in Figure 11, reveals the same shedding mechanism as that of lower *Re*. A single dominating frequency of the lift signal, shown in Figure 12 precludes the possibility of a pairwise shedding at this *Re*. Occurrence of inviscid critical points are considerably different at this *Re* with a number of saddles and centres are found to coexist in the presence of strong wavering of the wake which widens considerably from lower *Re*. Vorticity snapshots of Figure 11 shows increased motion of the region with concentrated vorticity at the rear end. The extent of bending of neck of the vortices that form at the vertices increase with the main body along with its tip shows marginal squeezing. Present results for $Re = 200$ and 250, in which range a three-dimensional wake transition can be expected, is at best can be regarded as the predictions at two-dimensional limit. A detailed three-dimensional calculations is needed to explore the three-dimensional nature of the flow at moderate *Re*.

4.4. Force coefficients and Strouhal number

Figure 13 shows how the integral parameters, namely C_D, C_L, $C_{L\mathrm{rms}}$ and Strouhal number change with *Re*. In the subcritical range ($Re < Re_{cr}$) C_D decreases as *Re* reaches the critical value (Figure 13(a)) due to diminishing effect of viscous force, a fact found in square cylinder configuration also. It should be noted that at this range of *Re* viscous drag dominates over the form drag and as *Re* reaches the critical value pressure drag becomes increasingly

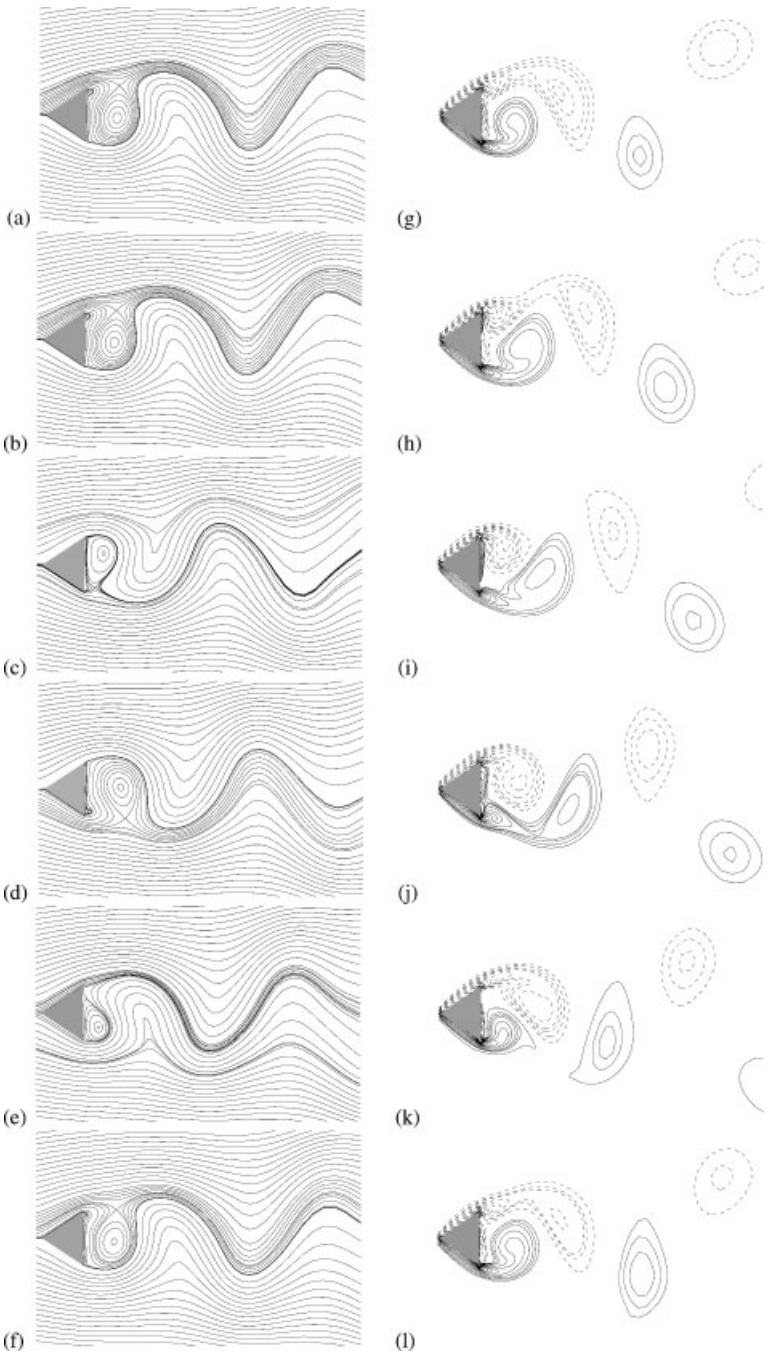

Figure 10. Equispaced $(\theta/6)$ snapshots within a shedding cycle, $Re = 200$.

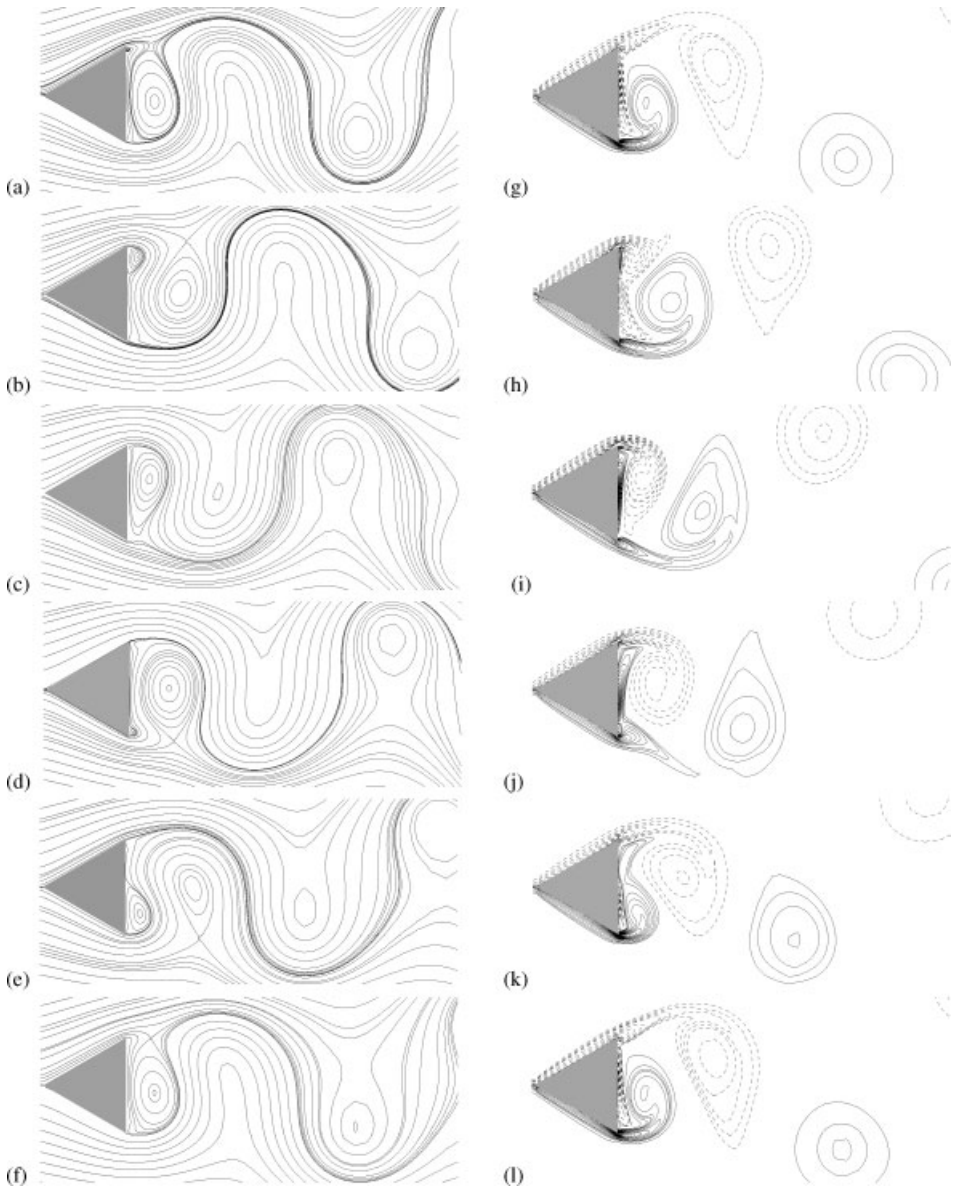

Figure 11. Equispaced $(\theta/6)$ snapshots within a shedding cycle, $Re = 250$.

important. In contrast to the square cylinder configuration, drag coefficient has been found to be an increasing function with Re above Re_{cr} as shown in Figure 13(b). This can be attributed to the streamlined shape of the triangular cylinder which facilitates formation of a thin boundary layer on the surfaces facing the incoming flow. Pressure drag coefficient follows the same trend as the total drag as with the increase in Re the size of the wake increases.

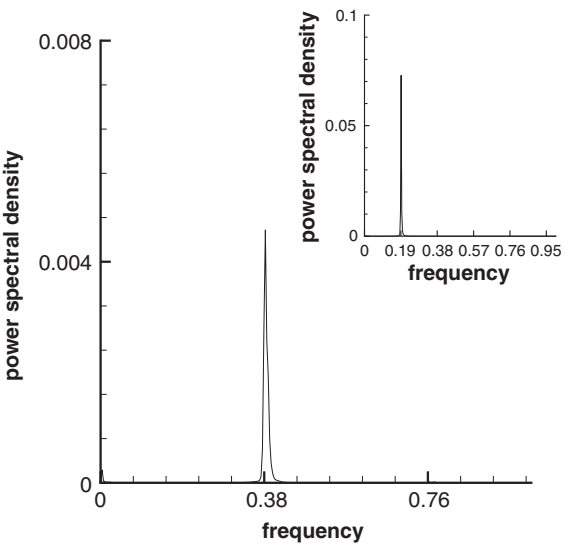

Figure 12. Fundamental frequency of the Drag and Lift coefficient (shown in the inset) signal at $Re = 250$.

The difference between these two coefficients, a measure of the friction drag, does not change appreciably in the range of Re studied in the present work. At all Re studied here, dominant frequency of drag coefficient has been seen to be twice that of the lift coefficient. This is shown in Figure 12 for $Re = 250$ where power spectrum density (PSD) of the drag coefficient has been shown in inset. Variation of Strouhal number with Re has been shown in Figure 13(c). The frequency of vortex shedding increases linearly with Re which is prolonged to $Re/Re_{cr} \approx 2$, a fact observed by Kahawita and Wang [32] in their computations for trapezoidal bluff bodies. Further increase in Re causes the curve to increase at a slower rate until it reaches a flat maximum at around $Re = 150$. After this maximum is reached, the frequency of shedding falls of. This interesting behaviour was also observed in the experiments of Okajima [33].

4.5. *Pathlines and streaklines*

Figure 14 shows the trajectories of particles released ahead of the cylinder. Particles have been tracked by integrating the Lagrangian description

$$\frac{\mathrm{d}\mathbf{x}(t)}{\mathrm{d}t} = \mathbf{u}(\mathbf{x}, t)$$

While particles are time-advanced using a second-order accurate time integration technique, velocities are interpolated from the neighbouring cells. It is apparent from the figure that with the increase in Re, wake containing the von Kármán vortex street widens showing the extent of transverse transport which scales with the dominating large vortical structures. Particles hardly move to the central zone of the wake as they mainly traverse along the edge of the wake. A variety of residence time of different particles are revealed as the particles entering

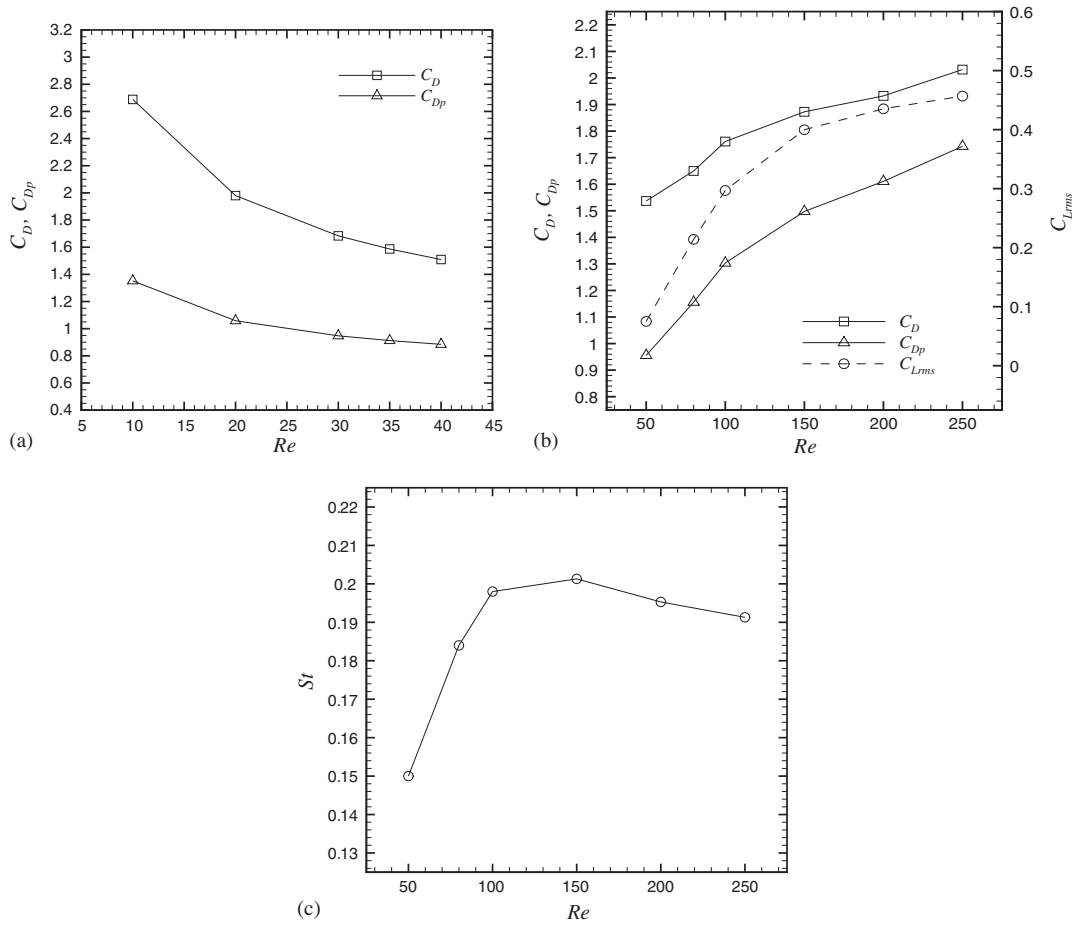

Figure 13. Integral parameters: (a) C_D and C_{D_p} for $10 \leqslant Re \leqslant 40$; (b) C_D, C_{D_p} and $C_{L_{\rm rms}}$ for $50 \leqslant Re \leqslant 250$; and (c) St.

close to the centreline are often bound for a long period in the near wake where vortices are forming.

Instantaneous streaklines generated using the tracked particles are shown in Figure 15. The particles are swept by the vortices and shed into the von Kármán vortex street. This is an excellent means of visualization as it clearly shows the alternate structure of shed vortices in the wake. Indeed, the spiral arrangement of the particles are the location of concentrated vorticity as can be seen from vorticity contours of Figures 8–11. As Reynolds number is increased, vorticity concentration is found to be increasingly localized in the near wake while the vortices spread in the far wake region. Also with the increase in *Re*, particle paths become more and more disorganized. At all Reynolds number studied in the present work, vortices are found to be shed alternately from top and bottom vertices of the cylinder with no evidence

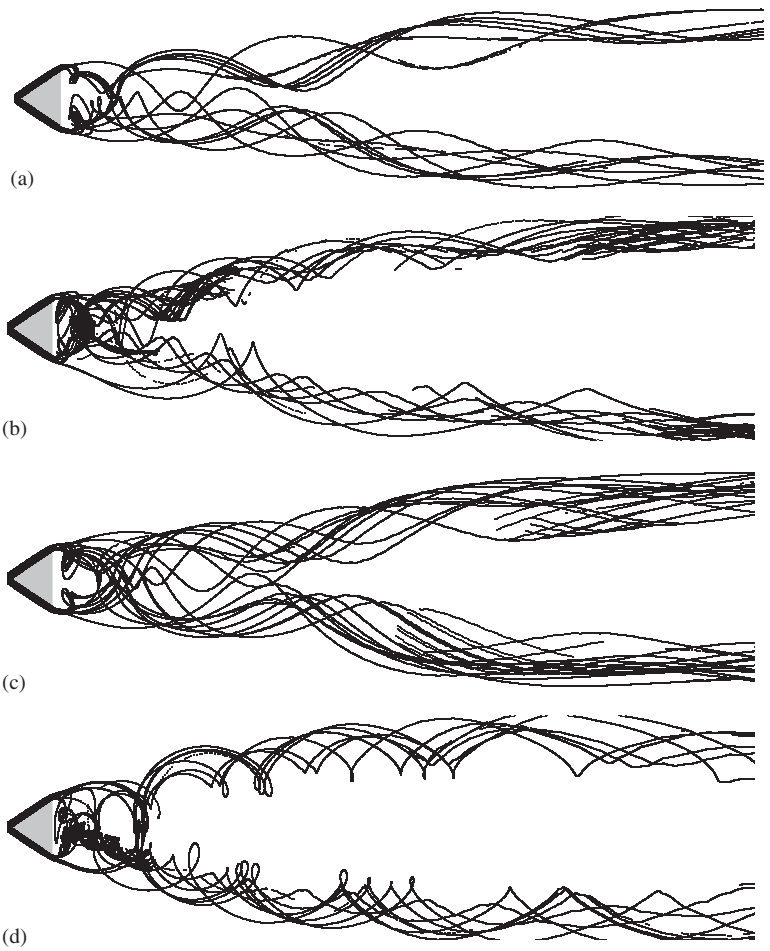

Figure 14. Particle trajectories: (a) $Re = 100$; (b) $Re = 150$; (c) $Re = 200$; and (d) $Re = 250$.

of pairwise shedding even at $Re = 250$. This fact is further evident form the single-frequency spectrum of the lift coefficient signal shown in Figure 12.

5. CONCLUSIONS

We have presented numerical simulations of two-dimensional laminar flow past a triangular cylinder. A multiblock finite volume method has been developed to numerically integrate the unsteady governing equations. Basing on the simulation results we conclude the following.

Global modes of u and v velocities give a critical Reynolds number of 39.9 which is close to some earlier results. Test for effect of domain size shows that changes in the solution is considerable working with lower downstream length. However, after a certain length solution ceases to change. At the subcritical Re, reattachment length follows a linear relationship with

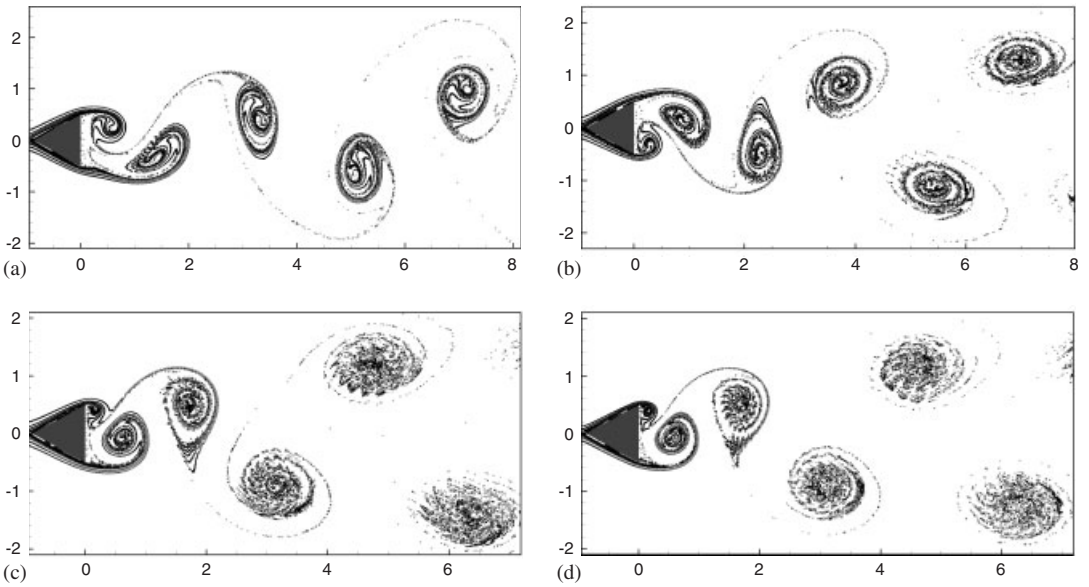

Figure 15. Instantaneous streaklines: (a) $Re = 100$; (b) $Re = 150$; (c) $Re = 200$; and (d) $Re = 250$.

Re. The vortex shedding mechanism is quite similar to the square cylinder case. However, the appearance of multiple frequency or pairwise shedding has not been observed even at $Re = 250$. Vortex shedding phenomena is associated with a flapping motion of the shear layer near the separation point. Particle trajectories and the streaklines provide a convenient means to visualize the wake. With the increase in *Re*, wavering motion of the wake becomes severe and the flow is more and more disorganized.

ACKNOWLEDGEMENTS

We have profited from the summer course by Prof. V. Eswaran at the institute which was precise and comprehensive. A word of thanks is due to Dr A. K. Saha for occasional discussion and help. Authors sincerely acknowledge the computing facility at CFD laboratory at the institute.

REFERENCES

1. Jordan SK, Fromm JE. Laminar flow past a circle in a shear flow. *Physics of Fluids* 1972; **215**:972–976.
2. Kiya M, Tamura H, Arie M. Vortex shedding from a circular cylinder in moderate Reynolds number shear flow. *Journal of Fluid Mechanics* 1972; **141**:721–735.
3. Braze M, Chassaing P, Ha Minh H. Numerical study and physical analysis of the pressure and velocity fields in the near wake of a circular cylinder. *Journal of Fluid Mechanics* 1990; **165**:79–130.
4. Zhang H, Fey U, Noack U. On the transition of the cylinder wake. *Physics of Fluids* 1995; **7**:779–794.
5. Williamson CHK. Vortex dynamics in the cylinder wake. *Annual Review of Fluid Mechanics* 1996; **28**:477–539.
6. Zdravkovich MM. *Flow Around Circular Cylinders*. Oxford University Press: New York, 1997.
7. Davis RW, Moore EF. A numerical study of vortex shedding from rectangles. *Journal of Fluid Mechanics* 1982; **116**:475–506.
8. Tamura T, Kuwahara K. Numerical study of aerodynamics behavior of a square cylinder. *Journal of Wind Engineering and Industrial Aerodynamics* 1990; **33**:161–170.

9. Okajima A. Numerical simulation of flow around rectangular cylinders. *Journal of Wind Engineering and Industrial Aerodynamics* 1990; **33**:171–180.
10. Kelkar KM, Patankar SV. Numerical prediction of vortex shedding behind a square cylinder. *International Journal for Numerical Methods in Fluids* 1992; **14**:327–341.
11. Sohankar A, Davidson L, Norberg C. Numerical simulation of unsteady flow around a square two-dimensional cylinder. *Proceedings of the 12th Australian Fluid Mechanics Conference*, Sydney, Australia, 1995; 517–520.
12. Saha AK, Biswas G, Muralidhar K. Three-dimensional study of flow past a square cylinder at low Reynolds numbers. *International Journal of Heat and Fluid Flow* 2003; **24**:54–66.
13. Sharma A, Eswaran V. Heat and fluid flow across a square cylinder in the two-dimensional laminar flow regime. *Numerical Heat Transfer Part A* 2004; **45**:247–269.
14. Jackson CP. A finite-element study of the onset of vortex shedding in flow past variously shaped bodies. *Journal of Fluid Mechanics* 1987; **182**:23–45.
15. Zielinska BJ, Wesfreid JE. On the spatial structure of global modes in wake flow. *Physics of Fluids* 1995; **7**:1418–1424.
16. Wesfreid JE, Goujon-Durand S, Zielinska BJ. Global mode behavior of the streamwise velocity in wakes. *Journal de Physique II* 1996; **6**:1343–1357.
17. Abbassi H, Turki S, Nasrallah SN. Numerical investigation of forced convection in a plane channel with a built-in triangular prism. *International Journal of Thermal Sciences* 2001; **40**:649–658.
18. Johansson SH, Davidson L, Olsson E. Numerical simulation of vortex shedding past triangular cylinders at high Reynolds number using a k–ε turbulence model. *International Journal for Numerical Methods in Fluids* 2005; **16**(10):859–878.
19. Roberts GO. Computational meshes for boundary layer problems. *Proceedings of the Second International Conference on Numerical Methods and Fluid Dynamics*, Lecture Notes in Physics. Springer-Verlag: New York, 1971; **8**:171–177.
20. Okajima A, Yi D, Sakuda A, Nakano T. Numerical study of blockage effects on aerodynamic characteristics of an oscillating rectangular cylinder. *Journal of Wind Engineering and Industrial Aerodynamics* 1997; **67**:91–102.
21. Sohankar A, Norberg C, Davidson L. Numerical simulation of unsteady low-Reynolds number flow around rectangular cylinders at incidence. *Journal of Wind Engineering and Industrial Aerodynamics* 1997; **69**:189–201.
22. Sohankar A, Norberg C, Davidson L. Simulation of three-dimensional flow around a square cylinder at moderate Reynolds numbers. *Physics of Fluids* 1999; **11**:288–306.
23. Sohankar A, Norberg C, Davidson L. Low-Reynolds number flow around a square cylinder at incidence: study of blockage, onset of vortex shedding and outlet boundary conditions. *International Journal for Numerical Methods in Fluids* 1998; **26**:39–56.
24. Orlanski I. A simple boundary condition for unbounded hyperbolic flows. *Journal of Computational Physics* 1976; **21**:251–269.
25. Yoshida T, Watanabe, Nakamura I. Numerical analysis of open boundary conditions for incompressible viscous flow past a square cylinder. *Transaction of JSME* 1993; **59**:2799–2806.
26. Sani RL, Gresho PM. Resume and remarks on the open boundary condition minisymposium. *International Journal for Numerical Methods in Fluids* 1994; **18**:983–1008.
27. Rudy DH. A nonreflecting outflow boundary condition for subsonic Navier–Stokes calculation. *Journal of Computational Physics* 1980; **36**:55–70.
28. Goujon-Durand S, Jenffer P, Wesfreid JE. Downstream evolution of the Bénard–von Kármán instability. *Physical Review E* 1994; **50**:308–313.
29. Dušek J, Le Gal P, Fraunie Ph. A numerical and theoretical study of the first Hopf bifurcation in a cylinder wake. *Journal of Fluid Mechanics* 1994; **264**:59–80.
30. Perry AE, Chong MS, Lim TT. The vortex shedding process behind two-dimensional bluff bodies. *Journal of Fluid Mechanics* 1982; **116**:77–90.
31. Eaton BE. Analysis of laminar vortex shedding behind a circular cylinder by computer-aided flow visualization. *Journal of Fluid Mechanics* 1987; **180**:117–145.
32. Kahawita R, Wang P. Numerical simulation of the wake flow behind trapezoidal bluff bodies. *Computers and Fluids* 2002; **31**:99–112.
33. Okajima A. Strouhal numbers in rectangular cylinders. *Journal of Fluid Mechanics* 1982; **123**:379–398.

